This article has been accepted for publication in IEEE Sensors Journal. This is the author's version which has not been fully edited and content may change prior to final publication. Citation information: DOI 10.1109/JSEN.2024.3402829

An 8-windows Continuous Wave Indirect Time-of-Flight Method for High Frequency SPAD-based 3D Imagers in 0.18 µm CMOS

François Piron, Hervé Pierre, and Jean-Michel Redouté, *Senior Member, IEEE*

***Abstract*— Time-of-flight (ToF) Single-Photon Avalanche Diode (SPAD) arrays are an increasingly popular option for 3D imaging. However, the traditional direct (dToF) and indirect (iToF) SPAD ranging pixels still struggle to get accuracies and precisons below the millimeter for short ranges. We propose to adapt the continuous-wave indirect time-of-flight (cw-iToF) method to use 8 integrating windows instead of the usual 4. This 8-windows cw-iToF method greatly reduces the non-linearity error when using a square optical signal, which consequently enables its use at much higher frequencies than if a sine wave was required, while also showing great robustness to an imperfect square wave, unlike pulse indirect time-of-flight (p-iToF). We provide an analysis of the effects of this new method on the accuracy and precision. Then, we present a single-pixel proof of concept implementation of an 8-taps cw-iToF SPAD pixel containing 4 up/down counters in a 0.18 µm CMOS process. Laser diodes illuminate the target with a 200 MHz square wave. The depth measurement's worst non-linearity error over a 75 cm range is 1.2 mm, and stays below one millimeter for more than 90% of the measured range. Furthermore, the precision for 100 ms-long frames is as low as 0.35 mm.**

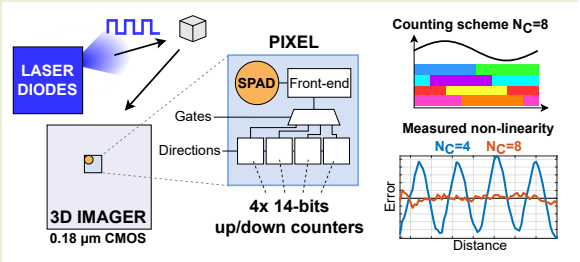

***Index Terms*— 3D camera, CMOS imager, Depth image sensor, Indirect Time-of-Flight (iToF), Continuous-wave indirect Time-of-Flight (cw-iToF), Time-Gated Single Photon Counting (TGSPC), Light Detection and Ranging (LiDAR), Time-of-Flight (ToF), Single-Photon Avalanche Diode (SPAD)**

I. Introduction

TIME-OF-FLIGHT (ToF) sensors infer the distance of an observed object by emitting a wave towards it with a known velocity, then measuring the time it takes the wave to come back. This wave can be a light pulse or signal generated by LEDs or lasers, and detected by photodetector cells on an integrated circuit (IC). If the receiver contains an array of independent pixels, each having photodetectors measuring time-of-flight, the depth of a whole scene can be mapped. The resulting device is effectively a 3D imager or camera.

Many other techniques exist to capture 3D images. Stereoscopic cameras use two 2D cameras physically separated from each other. Algorithms then process the images to recover depth, in the same manner human eyes do. This process is computationally intensive, and the quality of its results heavily depends on the contrast and clarity of the observed objects. These issues are avoided when light can be directly emitted by the device. Triangulation for example, shows great depth resolution and is robust in many environments where stereoscopic cameras would fail (e.g. in the dark or under direct sunlight). However, some sort of scanning is always required. On the other hand, monocular time-of-flight cameras provide a solid-state, effective and robust solution to depth imaging [1]–[4].

Time-of-flight ranging methods are divided in two categories: direct and indirect time-of-flight. Indirect time-of-flight (iToF) sensors measure the phase difference between the emitted optical wave, and the received signal in every pixel. Comparable to lock-in detection, this is accomplished by demodulating, or selectively accumulating the detected back-reflected signal electrically. Various iToF architectures have been proposed, often using CMOS or CCD photodetection followed by some way of gating and integrating the signal in a given number of taps [5], [6]. Depending on the shape of the emitted signal and the way of converting the raw values to phase, these methods belong to continuous-wave indirect time-of-flight (cw-iToF) or pulse indirect time-of-flight (p-iTof) [7], as shown in Fig. 1. In direct time-of-flight (dToF) systems, a short laser pulse is sent towards the observed scene. At the same moment, time-to-digital converters (TDC) or time-to-analog converters (TAC) in every pixel start measuring time like stopwatches, and stop when the pulse comes back to the sensor.

Single-Photon Avalanche Diodes (SPADs) are photodiodes reverse-biased over their breakdown voltage. In this unstable

The work of F. Piron was supported by a FRIA Grant funded by the FNRS, Belgium.

F. Piron, H. Pierre and J.-M. Redouté, are with the Department of Electrical Engineering and Computer Science, University of Liège, 4000, Belgium (francois.piron@uliege.be).

This article has been accepted for publication in IEEE Sensors Journal. This is the author's version which has not been fully edited and content may change prior to final publication. Citation information: DOI 10.1109/JSEN.2024.3402829

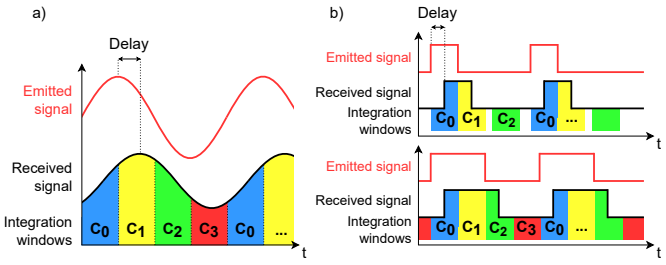

Fig. 1: Continuous wave (a) and pulse (b) iToF principles.

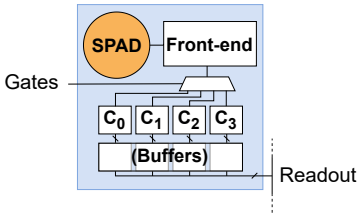

Fig. 2: Block diagram of a typical SPAD iToF pixel. The number of counters may vary depending on the chosen processing technique.

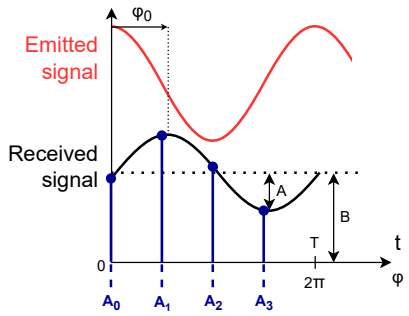

Fig. 3: Time diagram of the sampling of one period of the received signal.

state, there is a probability that an avalanche is triggered every time a photon hits the junction. With a circuit to sense and control this avalanche effect, SPADs thus provide a way to digitally detect discrete photon events [8], [9]. Thanks to their very high sensitivity and short reaction time, SPADs are particularly well suited for dToF pixel arrays, and the chosen photodetector for the vast majority of them. Nonetheless, iToF imagers can also benefit from the interesting properties of SPADs. The gating is digital and the integration is then obtained by counting photons. This method is referred to as time-gated single photon counting (TGSPC). A typical architecture of a SPAD iToF pixel is shown in Fig. 2.

A possible way to achieve the best depth imaging resolution over a short range using iToF is to increase the optical signal modulation frequency. Both non-linearity and precision errors are proportional to the range and will decrease accordingly. However, emitting an optical analog signal at 100's of MHz is not trivial. Typical modulated current driven LEDs will have physical rise and fall times in the order of 10 ns at best, impairing a precise distance measurement. The fastest commercially available LEDs have maximum modulation bandwidths of a few tens of MHz and only some state-of-the-art LEDs can be modulated at hundreds of MHz [10]. Laser diodes are faster, with widespread models easily modulated well above 100 MHz. However, they are hard to modulate with a high frequency analog signal at high output power, hence square waves are preferred. Considering all the the emitter-to-photodetector chain non-idealities, the resulting waveform will resemble an imperfect, filtered square, which is neither ideal for p-iToF, nor for cw-iToF.

In Section II, we propose an 8-windows cw-iToF processing method to alleviate this waveform issue at high modulation frequencies. The theoretical improvements on the precision, and on the non-linearity are elaborated respectively in Sections III and IV. The experimental setup is detailed in Section V, and the measurement results are presented in Section VI. Finally, in Section VII, we discuss the 8-windows cw-iToF method's performance, along with a comparison with existing time-of-flight sensor arrays, and provide insight about the potential place of iToF in the future of 3D cameras.

II. Method Presentation

The typical cw-iToF method often used in the literature [11], [12] computes the following calculation from the photon counts of 4 distinct integration windows to estimate phase shift:

$$\varphi' = \operatorname{atan}\left(\frac{C_1 - C_3}{C_0 - C_2}\right). \tag{1}$$

If we consider that the C_k's represent four exact samples of a sinusoidal signal, separated by a quarter period, implying $C_k = A_k$ on Fig. 3, this expression gives its exact phase. But it remains exact if the C_k values are obtained through the integration of the received signal in fixed-width windows [13], which is what happens in practice in iToF measurement systems over a large number of periods.

To be able to benefit from cw-iToF advantages at high frequencies, even with a square or not perfectly defined optical signal shape, and obtain excellent precision, this work introduces a cw-iToF depth estimation method with 8 integration windows. The photon counts are collected similarly to classical cw-iToF, but the signal period is divided into 8 distinct integration windows instead of the usual 4.

The updated estimation formula can be derived, starting from the original sample definition shown in Fig. 3, generalized below to an arbitrary number of windows N_C:

$$A_k = B + A\cos\left(\varphi_0 - k\frac{2\pi}{N_C}\right). \tag{2}$$

With $N_C = 8$, the following combination gives the phase shift using the contribution of all 8 samples:

$$\varphi_0 = \operatorname{atan}\frac{\sin\varphi_0}{\cos\varphi_0},$$

This article has been accepted for publication in IEEE Sensors Journal. This is the author's version which has not been fully edited and content may change prior to final publication. Citation information: DOI 10.1109/JSEN.2024.3402829

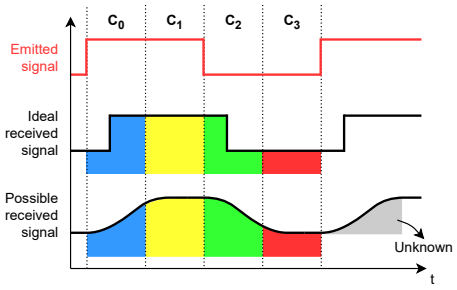

Fig. 4: Illustration of p-iToF issue with deformed optical signal shape. Counted values are no longer linear relative to phase shift.

where $\frac{\sin\ \varphi_0}{\cos\ \varphi_0}$ is given by:

$$\frac{\overbrace{2A\ \sin\ \varphi_0}^{A_2-A_6}+\frac{\sqrt{2}}{2}(\overbrace{\sqrt{2}A(\sin\ \varphi_0+\cos\ \varphi_0)}^{A_1-A_5}+\overbrace{\sqrt{2}A(\sin\ \varphi_0-\cos\ \varphi_0)}^{A_3-A_7})}{\underbrace{2A\ \cos\ \varphi_0}_{A_0-A_4}+\frac{\sqrt{2}}{2}(\underbrace{\sqrt{2}A(\cos\ \varphi_0+\sin\ \varphi_0)}_{A_1-A_5}+\underbrace{\sqrt{2}A(\cos\ \varphi_0-\sin\ \varphi_0)}_{A_7-A_3})}.$$

The estimation formula thus becomes:

$$\varphi' = \operatorname{atan}\left(\frac{C_2 - C_6 + \frac{\sqrt{2}}{2}(C_1 - C_5 + C_3 - C_7)}{C_0 - C_4 + \frac{\sqrt{2}}{2}(C_1 - C_5 + C_7 - C_3)}\right). \quad (3)$$

As explained in the following sections, these additional photon counts will lead to an improved depth uncertainty and non-linearity, even more so when the optical signal is square or square-like at high frequencies.

Increasing the amount of integration windows for iToF systems to mitigate the optical signal shape deformation occurring at higher frequencies would only be applicable to cw-iToF. For p-iToF, the additional counters would not be able to bring additional useful information. As shown in Fig. 4, the depth information is concentrated at the signal transitions, which are ideally inside a single integrating window at a time. Otherwise, the linear relation between the counted values and phase shift is lost. Without a predictable and constant optical signal shape, it would not be possible to compensate for it by using additional windows.

In order to take advantage of this 8-windows cw-iToF method, one might either count sequentially over different windows, or include additional counters inside the pixel's circuitry. Counting sequentially in 4 windows at a time, but keeping the same total integration length, will allow to benefit from the non-linearity improvement of the 8-windows method, but will give the same precision as for 4-windows cw-iToF. Currently, large process nodes are required to build and operate CMOS SPADs (40 nm at best, as reported in [14], [15]). Thus, a common issue with SPAD-based ToF pixels is their size, both for the SPAD cell itself as well as for the front-end and digital circuits. In this context, adding more counters, which will take up a significant area in each pixel, might not be desirable. The output bandwidth of the whole array will also need to scale according to the total amount of bits per pixel. Pixel pitch and data bandwidth are currently the main bottlenecks for large iToF arrays. These are some of the reasons explaining the rise of single-bit iToF SPAD pixel arrays [16], [17]. However, as smaller process nodes are progressively being used for SPAD pixels, the digital counters' contribution to the pixel size will become less significant. One might also expect higher data acquisition bandwidths, allowing the counters to be read more regularly, and thus to require less bits. Other solutions have also been tried, such as the use of two dies stacked on each other and connected by through-silicon vias (TSVs). One IC is manufactured in an appropriate technology node to host the SPADs, while the other IC can use a more advanced, smaller node so that the pixel digital circuits size becomes negligible [18], [19]. While this kind of method is currently very expensive and complex, it is reasonable to assume that such architectures will become more common in the future.

For iToF depth measurements, the maximum unambiguous range $\frac{T\times c}{2}$ is proportional to the illumination signal period T, where c is the speed of light. If the light signal travels more than one wavelength while performing its round-trip from the source, to the object and then back to the ToF sensor, the measured depth will be offset by a multiple of this range. As an example, a 50 MHz signal can be used to measure depth up to around 3 m. This range can be offset if the approximate depth is already known, or extended by performing multiple measurements with different illumination signal frequencies [20], [21]. The resolution or precision on the measured depth will also follow the signal period.

When comparing this new 8-windows cw-iToF method, the optical signal waveform is the error source that shows the greatest improvement, as will be detailed in Section IV.

III. Depth Precision

First, iToF RMS depth precision, σ_e can be linked to phase resolution σ_φ as such:

$$\sigma_e = \frac{R_D}{2\pi} \times \sigma_\varphi = \frac{c}{4\pi f_0} \times \sigma_\varphi, \quad (4)$$

where the non-ambiguous distance range R_D depends on the speed of light c and the optical modulation frequency f_0. The interest in increasing the modulation frequency to improve precision is already very clear, even though the maximum non-ambiguous range of the detector will decrease.

A. Uncertainty analysis

Now the phase resolution σ_φ can be analyzed in more detail. By using uncertainty propagation, one can derive how the detected photon count variance influences the error on the measured depth. This was done in [13] and [12] for cw-iToF with 4 sampling points. Photon counts C_k are considered independent, and assumed high enough to neglect higher-order terms in the Taylor expansion. An expression for the RMS phase resolution σ_φ was derived starting from:

$$\sigma^2_{\varphi'} = \sum_{k=0}^{N_C-1} \left|\frac{\partial \varphi}{\partial C_k}\right|^2 \sigma^2_{C_k}. \quad (5)$$

The derivatives are computed from (1). The different photon counts are considered to be Poisson random variables, so their variance is estimated by $\sigma^2_{C_k} = \mathbb{E}(C_k)$.

This article has been accepted for publication in IEEE Sensors Journal. This is the author's version which has not been fully edited and content may change prior to final publication. Citation information: DOI 10.1109/JSEN.2024.3402829

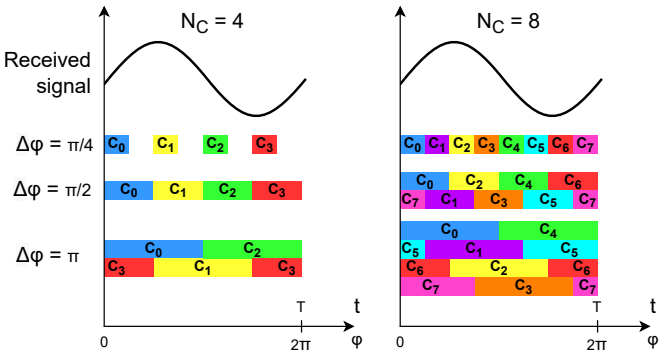

Fig. 5: Illustration of different integration widths $\Delta\varphi$.

We must consider that photon counts C_k are not samples of the optical signal but rather obtained by integrating this signal during the integration windows. This introduces a new parameter : the integration windows width $\Delta\varphi$. The expected photon counts are computed as such:

$$\begin{aligned}\mathbb{E}(C_k) &= B\Delta\varphi + A\int_{\varphi_0}^{\varphi_0+\Delta\varphi}\cos\left(x - k\frac{2\pi}{N_C}\right)\mathrm{d}x \qquad (6)\\ &= B\Delta\varphi + A\left[\sin\left(\varphi_0 - k\frac{2\pi}{N_C}\right)\right.\\ &\qquad \left. - \sin\left(\varphi_0 + \Delta\varphi - k\frac{2\pi}{N_C}\right)\right].\end{aligned}$$

Computing the analytical precision for $N_C = 4$ and $N_C = 8$ for different integration windows widths results in the values given in Table I.

TABLE I: Analytical phase error variance σ_φ^2

$\Delta\varphi$	σ_φ^2 $N_C = 4$	σ_φ^2 $N_C = 8$
$\pi/4$		$\frac{2+\sqrt{2}}{2}\frac{\pi B}{16A^2}$*
$\pi/2$	$\frac{\pi B}{8A^2}$*	$\frac{\pi B}{16A^2}$
π	$\frac{\pi B}{8A^2}$	$\frac{\pi B}{16A^2}$

*All received photons are accounted for once: $\Delta\varphi \times N_C = 2\pi$

Important conclusions can be extracted from these results. First, there is no difference between half-period and quarter-period windows ($\Delta\varphi = \pi/2$ and π), both for 4 and 8 counters. In practice, both could be chosen. Larger windows might be slightly easier to implement on-chip, but as each photon is counted twice, the counters will overflow or fill up sooner. Also, as expected, for these two window widths, the 8-taps method shows an improved error variance with a factor 2, and consequently taking $N_C = 8$ instead of 4 improves the theoretical depth precision by a factor $\sqrt{2}$. Finally, for $N_C = 8$, exactly dividing the period into 8 windows with a $\Delta\varphi = \pi/4$ width (full coverage without overlap) will lead to a 1.7 times larger variance than with wider integration windows. Regardless of the windows configuration, the precision is directly affected by the received background level $(B-A)$ and the signal amplitude A. These can be improved by optimizing the SPAD main characteristics: photon detection probability (PDP), fill factor and dark count rate (DCR), as well as the emitted power and SNR of the entire optical chain [8].

B. Verification by statistical simulation

A Monte-Carlo simulation has been developed to confirm the analytical expressions of Table I. This simulation statistically determines the number of photons in each counter, assuming these follow a Poisson distribution, depending on the optical wave shape and power level, the background power level and the photon detection efficiency. As the resulting variance is always a multiple of $\frac{B}{A^2}$, the results, shown in Table II, are expressed as relative values.

TABLE II: Numerically-computed relative depth error standard deviation

$\Delta\varphi$	σ'_φ $N_C = 4$	σ'_φ $N_C = 8$
$\pi/8$	1.83	1.29
$\pi/4$	1.31	0.93*
$\pi/2$	1*	0.707
π	1	0.710

*All received photons are accounted for once: $\Delta\varphi \times N_C = 2\pi$

The obtained standard deviations match the analytical values obtained before.

Simulations were also performed for shorter integration windows, with $\Delta\varphi \times N_C < 2\pi$. In these instances, some detected photons do not fall in any integration window and are ignored. Unsurprisingly, this deteriorates the precision.

IV. Aliasing / Non-linearity due to Optical Waveform Harmonics

When the illumination waveform is not perfectly sinusoidal and harmonics are introduced, a non-linear error appears in the cw-iToF measured depth because of aliasing, impairing the sensor's accuracy. This error can be computed for any signal shape by analysing how each harmonic of the signal spectrum is integrated and sampled in each tap, and then computing the effect on the estimated phase. The full development for 4 windows can be found in [13].

First, the signal containing the main frequency as well as the harmonics is analytically convoluted with a square wave representing the integration windows of the counters. This translates, in the frequency domain, into a multiplication with

$$\mathrm{sinc}(\pi f \Delta t) = \mathrm{sinc}\left(\pi\frac{f}{f_0}\frac{\Delta t}{T}\right), \qquad (7)$$

where $\frac{f}{f_0}$ represents the harmonic order and $\frac{\Delta t}{T} = \frac{\Delta\varphi}{2\pi}$ is the integrating window width ratio. Then, the signal is periodically sampled by the counters, at a sampling frequency of $N_C f_0$, through a convolution in frequency domain with

$$\sum_{k=-\infty}^{+\infty}\delta(kN_c f_0). \qquad (8)$$

This article has been accepted for publication in IEEE Sensors Journal. This is the author's version which has not been fully edited and content may change prior to final publication. Citation information: DOI 10.1109/JSEN.2024.3402829

TABLE III: Harmonics-induced phase estimation error

Input signal		Phase error		Max phase error	
		N_C=4	N_C=8	N_C=4	N_C=8
Sine	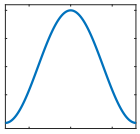	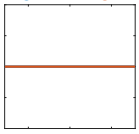		0	0
Square	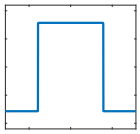	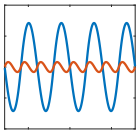		1.13%	0.13%
Square first 4 harmonics	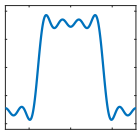	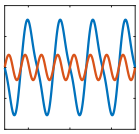		1.23%	0.32%
Filtered square	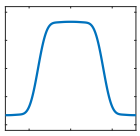	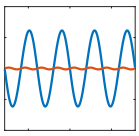		0.98%	0.02%

Finally, the phase of the expression is evaluated at $f = f_0$ to obtain the phase that will effectively be extracted from the counters measurements.

This reasoning has been adapted to compare the phase error with the proposed 8 counters method. Instead of only rejecting the even harmonics like its 4-tap counterpart, the proposed method rejects 3/4 of them, keeping the 7th, 9th, 15th, 17th, 23rd, etc. The square wave lower-order odd harmonics have the highest amplitude and are thus the most influential on the non-linearity error. Therefore, as the 3rd and 5th harmonics are rejected with $N_C = 8$, aliasing will be significantly reduced. The theoretical aliasing phase errors for a few illumination waveforms are shown in Table III. The eliminated harmonics are identical for $\Delta\varphi = \pi$ and $\Delta\varphi = \pi/2$.

Although this error can be reduced by calibration for a known waveform, e.g. using a look-up table, this will not be effective in a real environment with an illumination signal shape that is not perfectly known and that varies due to echo/multi-path effects, reflectivity variation, temperature dependence of the emitter and of the SPADs, and various other uncontrollable factors. A much lower error on the raw estimation also guarantees a better final accuracy after calibration.

V. Experimental Setup

A prototype IC was designed and fabricated in a 0.18 µm CMOS process, containing depth sensor pixels in various configurations. A micrograph is shown in Fig. 6. As the prototype SPAD cells had not been previously tested, multiple designs were included in the layout. Measurements were performed on a single pixel, whose architecture is depicted in Fig. 2, excluding the memory buffers. The pixel was selected based on its measured SPAD and front-end performance. It contains a SPAD with an active area of 11.6 µm^2, and 992 µm^2 of total area including the guard ring. Its front-end utilizes a passive quenching and recharge circuit. The SPAD cell chosen for the measurements presented in this paper has a measured

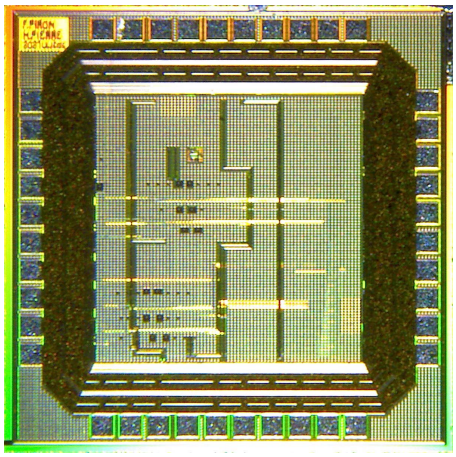

Fig. 6: Micrograph of the prototype IC, fabricated in a 0.18 µm CMOS process. Its total size is 1.5 mm × 1.5 mm.

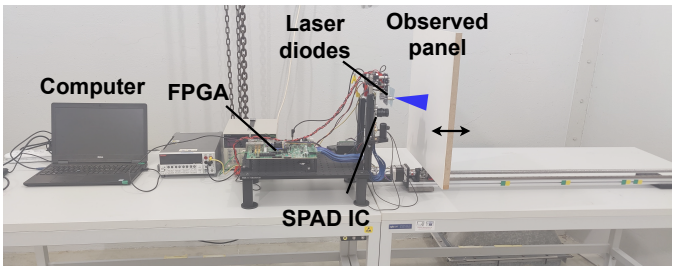

Fig. 7: Annotated picture of the experimental setup.

photon detection probability (PDP) of 6.2% at 450 nm and a dark count rate (DCR) of around 12 kHz. Then, the signal is routed to the appropriate counters, of which the gating and counting direction is determined by external clock signals. The pixel contains 4 linear-feedback shift register (LFSR) 14-bit counters, capable of counting in both directions. Counting is automatically paused as soon as one of the counters hits an overflow value. After the data is flushed, the counting resumes. For a fully developed sensor, the 4 up/down counters would be always active during exposure, but with their direction sequentially changing, effectively achieving the $\Delta\varphi = \pi$ scheme illustrated in Fig. 5. In the context of the experiments presented in this paper, due to high-speed reliability issues with some of the counters, the count values are obtained sequentially. Finally, 3-state buffers transfer the acquired data to output registers, allowing it to be extracted and processed by an FPGA development board.

As explained above, a higher optical modulation frequency leads to a better depth resolution and accuracy. The aim is then to reach the highest possible modulation frequency, as long as the clocks and counters still reliably work, and the laser source can still be modulated with the highest possible modulation coefficient. Reasonable jitter is not an issue as filtering the square signal will reduce its harmonics, but the asymmetry of the emitted signal should be kept to a minimum. The presented setup operates with a 200 MHz square wave, which represents a significant increase compared to similar existing SPAD cw-iToF systems. Unavoidably, the unambiguous max range is limited to 75 cm, but is extendable using multiple frequencies.

This article has been accepted for publication in IEEE Sensors Journal. This is the author's version which has not been fully edited and content may change prior to final publication. Citation information: DOI 10.1109/JSEN.2024.3402829

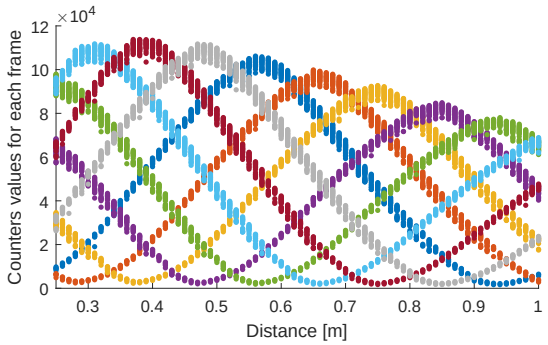

Fig. 8: Counters absolute values over measuring range, for the 200 MHz modulation frequency. A total of 1000 frames of 100 ms length were captured for each distance. Each point represents a single frame. Each color represents one of the 8 counters.

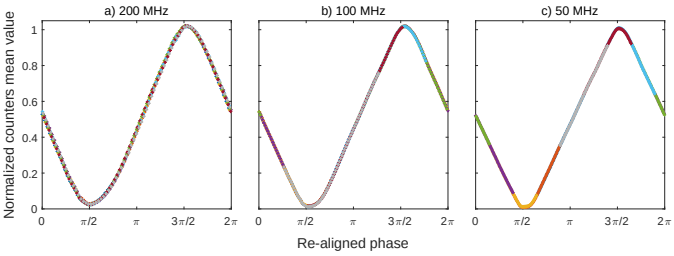

Fig. 9: Received signal shape, reconstructed by realigning and normalizing all counter values. Each color represents one of the 8 counters.

Due to the physical nature of LEDs, such modulation frequencies are not attainable [10], so laser diodes have been chosen instead. The use of laser diodes constrains the optical signal to have a square waveform. The optical emitter is based on 9 diffused blue 450 nm laser diodes, all driven by the same modulation signal. Each of them has a peak output power of 100 mW, resulting in a total 900 mW maximum optical power. The room is darkened during measurements. Also, its temperature is kept stable, as preliminary testing showed non-negligible delay drifts during multiple hours-long statistical data accumulation due to changing room temperature. This would not be an issue at multiple frames per seconds, as the offset can be measured and corrected during the depth estimation. The laser diodes are unfocused, with a typical divergence of 22 degrees by 6.5 degrees. However, they are placed in a circle, resulting in a star-shaped beam, which roughly approaches a circular beam shape, after a diffuser sheet.

An F1.4 12 mm camera lens is mounted in front of the sensor. The observed object is a white wood panel placed on a motorized rail to precisely travel to different known distances. The setup, shown in Fig. 7, is automated and controlled remotely.

VI. Experimental Results

A constant offset is added to the measurements, but no other calibration is performed. The resulting raw data at 200 MHz is shown in Fig. 8. For each frame, the value of the 8 counters are

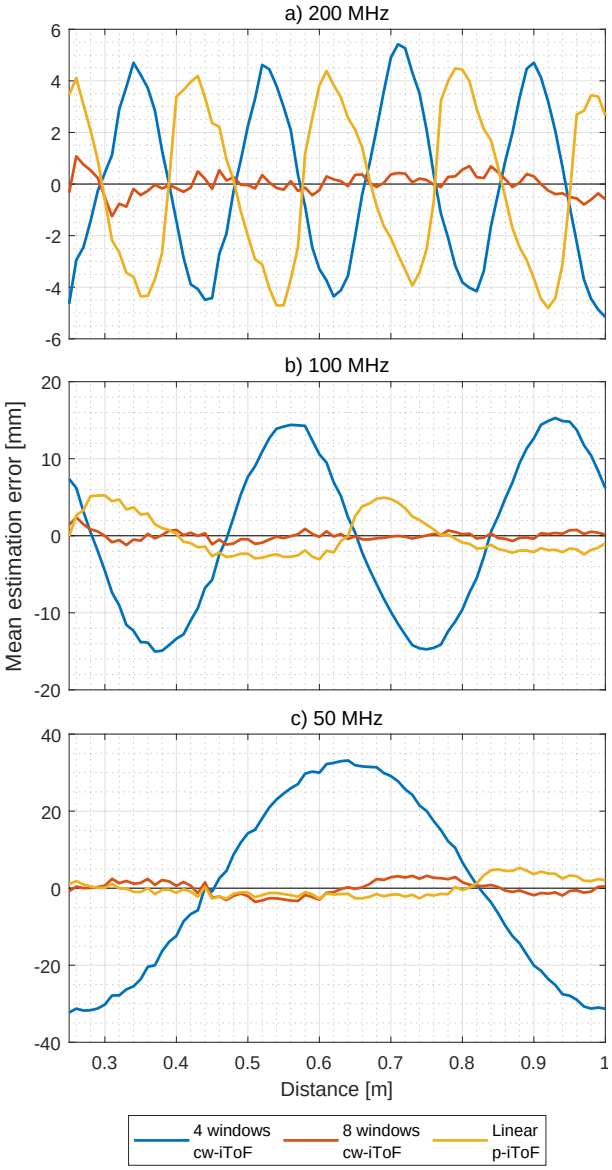

Fig. 10: Estimation bias / non-linearity over the measuring range for different modulation frequencies. A total of 1000 frames of 100 ms length were captured for each distance.

plotted in different colors. These raw counts give an average demodulation contrast coefficient (measured $\frac{A}{B}$ ratio) of 95%. From this data, the relative waveform of the received signal can also be retrieved. Each value is normalized by the average received optical power at that distance. Then, the waveform of each counter is shifted to remove their phase difference. This results in the waveforms shown in Fig. 9. The presented shape represents the convolution of the optical signal with the integration window. As the counters integrate the 50% duty cycle optical signal during half periods, a perfectly square laser signal would yield a triangular shape. As expected, the received signal is closer to a square at 50 MHz. It smoothens at higher frequencies, due to timing jitter and the rise and fall times of the laser emitters.

The accuracy results are shown in Fig. 10 and Table IV. The worst accuracy, without calibration, for the proposed 8-

This article has been accepted for publication in IEEE Sensors Journal. This is the author's version which has not been fully edited and content may change prior to final publication. Citation information: DOI 10.1109/JSEN.2024.3402829

TABLE IV: Worst measured accuracy over the measuring range, expressed in absolute value and in phase error percentage. Corresponds to the absolute maximums of the curves in Fig. 10

	4 windows cw-iToF	8 windows cw-iToF	Linear p-iToF
200 MHz	5.4 mm 0.7%	1.2 mm 0.16%	4.8 mm 0.64%
100 MHz	15.3 mm 1.02%	2.4 mm 0.16%	5.2 mm 0.35%
50 MHz	33.2 mm 1.11%	3.6 mm 0.12%	5.3 mm 0.18%

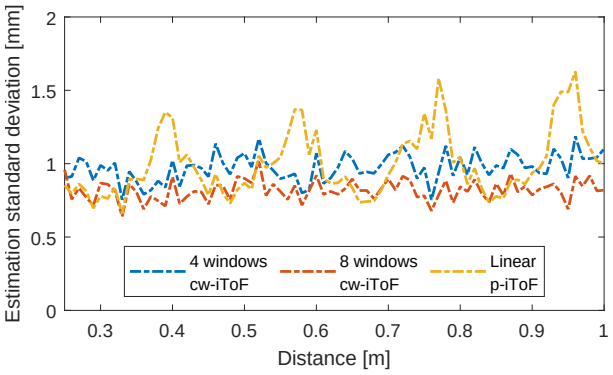

Fig. 11: Precision (standard deviation of estimation) over measurement range, with a 200 MHz modulation frequency. A total of 1000 frames of 100 ms length were captured for each distance.

windows cw-iToF method at 200 MHz is 1.2 mm, and the accuracy stays below one millimeter for all distances greater than 31 cm.

One can observe on Fig. 10 that the shape of the cw-iToF non-linearity follows the theory of harmonics-induced phase errors, presented in Section IV, because of the square laser signal. As previously computed, the 4-windows method is a lot more prone to this error source. With 8 windows, the worst accuracy is 9 times better at 50 MHz and 4.5 times better at 200 MHz.

The linear calculation method, on the other hand, expects a square wave. The non-linearity error is thus lower at slower modulation frequencies, and becomes predominant when the waveform becomes rounder at higher modulation frequencies.

The standard deviations of the distance estimations at 200 MHz are plotted in Fig. 11, and their average values are shown in Table V. For cw-iToF methods, it stays rather constant over the whole measured range. As provided in Section III, the standard deviation should only depend on the counted quantity of signal and background photons. The standard deviation ratio between the 4 and 8-windows methods is between 0.8 and 0.9, while the expected theoretical ratio derived in Table I is $\sqrt{2}/2 \approx 0.71$. The difference is explained by external factors impinging the precision of the system, such as imperfect motor displacement over all the cycles.

TABLE V: Average precision over the measuring range for 100 ms long frames, over a 5-day period, expressed in absolute value and in phase error percentage. Corresponds to the averages of Fig. 11

	4 windows cw-iToF	8 windows cw-iToF	Linear p-iToF
200 MHz	0.97 mm 0.13%	0.82 mm 0.11%	1.00 mm 0.13%
100 MHz	1.54 mm 0.10%	1.30 mm 0.09%	1.59 mm 0.11%
50 MHz	3.05 mm 0.10%	2.71 mm 0.09%	3.18 mm 0.11%

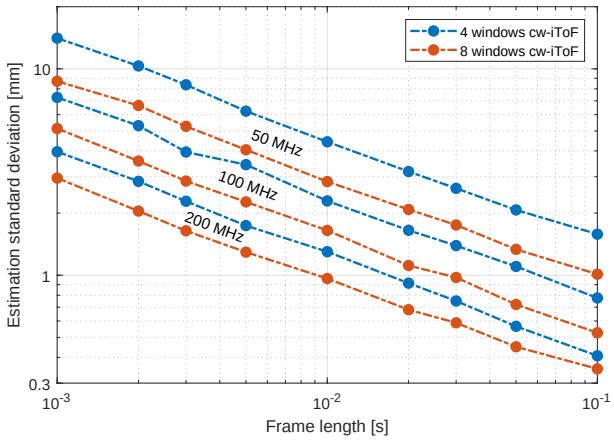

Fig. 12: Precision (standard deviation of estimation) in function of frame length. Each value has been computed on 1000 frames obtained with a constant observed distance of 0.4 m.

Another batch of data was recorded at a fixed distance of 0.4 m. The experiment lasted 6 days and measured distance using different frames lengths. Data for 100 ms frames is included in Table VI. While the conditions are identical to the results presented above, the standard deviation is significantly lower, going from 0.82 to 0.35 mm with the 8-windows estimator at 200 MHz. This significant improvement at a fixed distance shows that the first standard deviation is substantially affected by the motor movements, and more generally by our characterization setup.

Fig. 12 shows the effect of frame length on the precision.

TABLE VI: Average precision at fixed distance of 0.4 m for 100 ms long frames, expressed in absolute value and in phase error percentage. Corresponds to values of Fig. 12

	4 windows cw-iToF	8 windows cw-iToF
200 MHz	0.41 mm 0.05%	0.35 mm 0.05%
100 MHz	0.78 mm 0.05%	0.53 mm 0.04%
50 MHz	1.58 mm 0.05%	1.01 mm 0.03%

TABLE VII: Properties of a few time-of-flight sensor arrays

	This work	[12]	[22]	[15]	[23]	[24]	[14]	[25]
Photodetector	**SPAD**	SPAD	SPAD	SPAD	SPAD	Analog PD[a]	SPAD	SPAD
Method	**cw-iToF 8 taps**	cw-iToF 4 taps	PD$\Sigma\Delta$[b]	p-iToF	p-iToF	p-iToF	dToF (Gated RO[c])	dToF (RO[c])
Counters config [bits]	**4×14b u/d[d]**	2×8b	1×6b u/d[d] + 1×6b	2×16b	2× analog counters	2× charge accumulation	1×9b + 4b RO[c]	1×11b
Tech. node	**180 nm**	350 nm	130 nm	40 nm	110 nm	65 nm	40 nm	150 nm
Array size	**1 pixel**	60×48	128×96	128×128	64×64	1024×1024	192×128	50×40
Pixel area [µm×µm]	**75×75[e]**	85×85	44.65×44.65	40×20	32×32	3.5×3.5	18.4×9.2	38.5×33.5
Fill factor	**0.23%**	0.53%	3.17%	13%	26.3%	∼100%[f]	13%	4.8–15.3%
Front-end	**Passive**	PQAR[g]	Passive	Passive	Passive	–	Passive	Passive
Optical wavelength [nm]	**450**	850	850	840	850	860	654	650
Modulation frequency [MHz]	**200**	30	3.33	–	1.56 & 50	200	2 (pulses)	10 (pulses)
Max unambiguous range [m]	**0.75**	5	45	48	50	4	73.5	7.5
Range of measurement [m]	**0.75**	2.4	2.4	3	50	3.8	42	3
Frame length [ms]	**100**	45	50	10	15.4	33.3	0.054	1
Precision σ_{error} [mm]	**0.35**	38	160	64	11.3	2.2	62.4	1.6
Precision σ_{error} [% range]	**0.05%**	1.6%	6.7%	2.1%	0.02%	0.06%	0.15%	0.05%
Worst accuracy/INL $\lvert\mu_{\text{error}}\rvert$ [mm]	**1.2**	110	5	36	70	1.6	33	19
Worst accuracy/INL [% range]	**0.16%**	4.6%	0.21%	1.2%	0.14%	0.04%	0.08%	0.6%

[a]Photodetector [b]Phase-domain sigma-delta [c]Ring oscillator [d]Up/down [e]Equivalent pitch based on total area
[f]With microlenses [g]Passive quenching, active recharge

The empirical data follows

$$\sigma_\varphi \propto \frac{1}{\sqrt{T_e}}, \tag{9}$$

where T_e is the exposure time or frame length. This is consistent with the values in Table I, in which A and B are both proportional to T_e.

Note that the frame exposure length is not necessarily equal to the frame period (inverse of the frame rate), as depending on the implementation of the shutter, readout, and notably the presence or not of counter buffers, the pixel might not always be active.

VII. Discussion and Conclusion

The properties and measured performance of the presented 0.18 µm CMOS sensor are compared with other various time-of-flight arrays in Table VII. The high modulation frequency laser-generated square wave, in combination with a reduction of non-linearities by using 8 integration windows, enables excellent precision and accuracy of the measured depth. With some optimization on the SPAD cell itself, increasing its PDP, reducing its DCR and with a greater fill factor, these results could even be better.

Even though increasing the frequency shortens the unambiguous range, the presented method is particularly relevant for applications where precision and accuracy are more valuable than an extended range, such as in object recognition, robotics, or biomedical imaging. If required, the range can also be extended by using multiple frequencies.

Whereas the higher non-linearity in other sensors could be alleviated with calibration, some fluctuating parameters would still create unavoidable errors. For example, the temperature dependency of the shape of the received waveform is related to many effects, taking place both in the emitter and in the photodetector, making it hardly predictable and correctable in a practical usage environment. Therefore, the exceptionally low non-linearities of the presented method makes it very robust by design to these external effects.

Due to the need of more digital circuitry, and the typically large SPAD cells, iToF SPAD pixels are still much larger than those using analog photodetectors. Furthermore, doubling the number of counters per pixel to use cw-iToF with 8 simultaneous gated integrations will further increase the area requirements. However, we might expect the size of SPAD pixels to shrink substantially in the future, thanks to their availability in smaller process nodes, and the increasing usage of 3D ICs. Fill factor will also benefit from these improvements, in addition to microlens arrays which are already common in time-of-flight imagers.

At very short range, dToF SPAD pixels are still unable to provide the same level of absolute accuracy and precision as iToF ones. State-of-the-art short range dToF imagers only achieve accuracies in the centimeter range [14], [25], [26]. In-pixel direct time-to-digital converters and their embedded interpolators would also require unreasonably high frequencies in order to reach picosecond resolutions, already within reach of iToF imagers. Otherwise, the dToF array would need to work at higher pulse rates and process or output data with a huge bandwidth to gather enough measurements to get precise frames at a decent rate.

Although iToF SPAD arrays are still behind their analog photodetector counterparts in terms of pixel density, continuous progress in the large-scale integration of SPAD imagers is expected, with potential for more advanced in-pixel digital processing capabilities, ensuring their competitiveness for future short range 3D cameras.

REFERENCES

[1] M. Hansard, S. Lee, O. Choi, and R. P. Horaud, *Time-of-flight cameras: principles, methods and applications*. Springer Science & Business Media, 2012.

[2] F. Remondino and D. Stoppa, *TOF range-imaging cameras*. Springer-Verlag Berlin Heidelberg, Jul 2013.

[3] R. Horaud, M. Hansard, G. Evangelidis, and C. Ménier, "An overview of depth cameras and range scanners based on time-of-flight technologies," *Machine Vision and Applications*, vol. 27, no. 7, pp. 1005–1020, Oct 2016.

[4] F. Piron, D. Morrison, M. R. Yuce, and J.-M. Redouté, "A review of single-photon avalanche diode time-of-flight imaging sensor arrays," *IEEE Sensors Journal*, vol. 21, no. 11, pp. 12 654–12 666, 2021.

[5] C. Bamji, J. Godbaz, M. Oh, S. Mehta, A. Payne, S. Ortiz, S. Nagaraja, T. Perry, and B. Thompson, "A review of indirect time-of-flight technologies," *IEEE Transactions on Electron Devices*, vol. 69, no. 6, pp. 2779–2793, 2022.

[6] K. Yasutomi and S. Kawahito, "Lock-in pixel based time-of-flight range imagers: An overview," *IEICE Transactions on Electronics*, vol. E105.C, no. 7, pp. 301–315, 2022.

[7] S. Bellisai, F. Villa, S. Tisa, D. Bronzi, and F. Zappa, "Indirect time-of-flight 3D ranging based on SPADs," in *Proc. SPIE Quantum Sensing and Nanophotonic Devices IX*, vol. 8268, Jan 2012, pp. 282–289.

[8] D. P. Palubiak and M. J. Deen, "CMOS SPADs: Design issues and research challenges for detectors, circuits, and arrays," *IEEE Journal of Selected Topics in Quantum Electronics*, vol. 20, no. 6, pp. 409–426, 2014.

[9] D. Bronzi, F. Villa, S. Tisa, A. Tosi, and F. Zappa, "SPAD figures of merit for photon-counting, photon-timing, and imaging applications: A review," *IEEE Sensors Journal*, vol. 16, no. 1, pp. 3–12, 2016.

[10] A. Ren, H. Wang, W. Zhang, J. Wu, Z. Wang, R. V. Penty, and I. H. White, "Emerging light-emitting diodes for next-generation data communications," *Nature Electronics*, vol. 4, no. 8, pp. 559–572, 2021.

[11] R. Lange and P. Seitz, "Solid-state time-of-flight range camera," *IEEE Journal of Quantum Electronics*, vol. 37, no. 3, pp. 390–397, 2001.

[12] C. Niclass, C. Favi, T. Kluter, F. Monnier, and E. Charbon, "Single-photon synchronous detection," *IEEE Journal of Solid-State Circuits*, vol. 44, no. 7, pp. 1977–1989, 2009.

[13] R. Lange, "3D time-of-flight distance measurement with custom solid-state image sensors in CMOS/CCD-technology," Ph.D. dissertation, Universität Siegen, 2000. [Online]. Available: https://dspace.ub.uni-siegen.de/handle/ubsi/178

[14] R. K. Henderson, N. Johnston, F. Mattioli Della Rocca, H. Chen, D. Day-Uei Li, G. Hungerford, R. Hirsch, D. Mcloskey, P. Yip, and D. J. S. Birch, "A 192 × 128 time correlated SPAD image sensor in 40-nm CMOS technology," *IEEE Journal of Solid-State Circuits*, vol. 54, no. 7, pp. 1907–1916, 2019.

[15] F. Mattioli Della Rocca, H. Mai, S. W. Hutchings, T. A. Abbas, K. Buckbee, A. Tsiamis, P. Lomax, I. Gyongy, N. A. W. Dutton, and R. K. Henderson, "A 128 × 128 SPAD motion-triggered time-of-flight image sensor with in-pixel histogram and column-parallel vision processor," *IEEE Journal of Solid-State Circuits*, vol. 55, no. 7, pp. 1762–1775, 2020.

[16] N. A. W. Dutton, I. Gyongy, L. Parmesan, S. Gnecchi, N. Calder, B. R. Rae, S. Pellegrini, L. A. Grant, and R. K. Henderson, "A SPAD-based QVGA image sensor for single-photon counting and quanta imaging," *IEEE Transactions on Electron Devices*, vol. 63, no. 1, pp. 189–196, 2016.

[17] X. Ren, P. W. R. Connolly, A. Halimi, Y. Altmann, S. McLaughlin, I. Gyongy, R. K. Henderson, and G. S. Buller, "High-resolution depth profiling using a range-gated CMOS SPAD quanta image sensor," *Optics Express*, vol. 26, no. 5, pp. 5541–5557, Mar 2018.

[18] S. Parent, M. Côté, F. Vachon, R. Groulx, S. Martel, H. Dautet, S. A. Charlebois, and J.-F. Pratte, "Single photon avalanche diodes and vertical integration process for a 3D digital SiPM using industrial semiconductor technologies," in *Proc. IEEE Nuclear Science Symposium and Medical Imaging Conference*, 2018, pp. 1–4.

[19] T. Al Abbas, O. Almer, S. W. Hutchings, A. T. Erdogan, I. Gyongy, N. A. Dutton, and R. K. Henderson, "A 128×120 5-wire 1.96mm2 40nm/90nm 3D stacked SPAD time resolved image sensor SoC for microendoscopy," in *Proc. IEEE Symposium on VLSI Circuits*, 2019, pp. C260–C261.

[20] A. D. Payne, A. P. Jongenelen, A. A. Dorrington, M. J. Cree, and D. A. Carnegie, "Multiple frequency range imaging to remove measurement ambiguity," in *Proc. 9th Conference on Optical 3-D Measurement Techniques*, Jul 2009, pp. 139–148.

[21] P. F. Shahandashti, P. López, V. M. Brea, D. García-Lesta, and M. H. Conde, "Simultaneous multifrequency demodulation for single-shot multiple-path ToF imaging," *IEEE Transactions on Computational Imaging*, vol. 10, pp. 54–68, 2024.

[22] R. J. Walker, J. A. Richardson, and R. K. Henderson, "A 128×96 pixel event-driven phase-domain $\Delta\Sigma$-based fully digital 3D camera in 0.13μm CMOS imaging technology," in *Proc. IEEE International Solid-State Circuits Conference*, 2011, pp. 410–412.

[23] B. Park, I. Park, C. Park, W. Choi, Y. Na, M.-J. Lee, and Y. Chae, "A 64 × 64 SPAD-based indirect time-of-flight image sensor with 2-tap analog pulse counters," *IEEE Journal of Solid-State Circuits*, vol. 56, no. 10, pp. 2956–2967, 2021.

[24] C. S. Bamji, S. Mehta, B. Thompson, T. Elkhatib, S. Wurster, O. Akkaya, A. Payne, J. Godbaz, M. Fenton, V. Rajasekaran, L. Prather, S. Nagaraja, V. Mogallapu, D. Snow, R. McCauley, M. Mukadam, I. Agi, S. McCarthy, Z. Xu, T. Perry, W. Qian, V.-H. Chan, P. Adepu, G. Ali, M. Ahmed, A. Mukherjee, S. Nayak, D. Gampell, S. Acharya, L. Kordus, and P. O'Connor, "IMpixel 65nm BSI 320MHz demodulated TOF image sensor with 3μm global shutter pixels and analog binning," in *Proc. IEEE International Solid-State Circuits Conference*, 2018, pp. 94–96.

[25] M. Perenzoni, N. Massari, L. Gasparini, M. M. Garcia, D. Perenzoni, and D. Stoppa, "A fast 50 × 40-pixels single-point DTOF SPAD sensor with photon counting and programmable ROI TDCs, with σ <4 mm at 3 m up to 18 klux of background light," *IEEE Solid-State Circuits Letters*, vol. 3, pp. 86–89, 2020.

[26] C. Zhang, S. Lindner, I. M. Antolović, J. Mata Pavia, M. Wolf, and E. Charbon, "A 30-frames/s, 252×144 SPAD flash LiDAR with 1728 dual-clock 48.8-ps TDCs, and pixel-wise integrated histogramming," *IEEE Journal of Solid-State Circuits*, vol. 54, no. 4, pp. 1137–1151, 2019.